Water Stable 1D Hybrid Tin(II) Iodide Emits Broad Light with 36% Photoluminescence Quantum Efficiency

Ioannis Spanopoulos, Ido Hadar, Weijun Ke, Peijun Guo, Siraj Sidhik, Mikael Kepenekian, Jacky Even, Aditya D Mohite, Richard Schaller, Mercouri G Kanatzidis

Water Stable 1D Hybrid Tin(II) Iodide Emits Broad Light with 36% Photoluminescence Quantum Efficiency

Ioannis Spanopoulos[1], Ido Hadar[1], Weijun Ke[1], Peijun Guo[2#], Siraj Sidhik[5], Mikaël Kepenekian[3], Jacky Even[4], Aditya D. Mohite[5], Richard D. Schaller[1], and Mercouri G. Kanatzidis*[,1]

[1]*Department of Chemistry, Northwestern University, Evanston, IL 60208, United States*
[2]*Center for Nanoscale Materials, Argonne National Laboratory, 9700 South Cass Avenue, Lemont, Illinois 60439, United States*
[3]*Univ Rennes, ENSCR, INSA Rennes, CNRS, ISCR (Institut des Sciences Chimiques de Rennes), UMR 6226, Rennes F-35000, France*
[4]*Univ Rennes, INSA Rennes, CNRS, Institut FOTON, UMR 6082, Rennes F-35000, France*
[5]*Department of Chemical and Biomolecular Engineering, Rice University, Houston, TX 77005, United States*

ABSTRACT

The optical and light emission properties of tin and lead halide perovskites are remarkable because of the robust room temperature performance, broad wavelength tunability, high efficiency and good quenching-resistance to defects. These highly desirable attributes promise to transform current light emitting devices, phosphors and lasers. One disadvantage in most of these materials is the sensitivity to moisture. Here we report a new air-stable one-dimensional (1D) hybrid lead-free halide material (DAO)Sn_2I_6 (DAO: 1,8-octyldiammonium) that is resistant to water for more than 15h. The material exhibits a sharp optical absorption edge at 2.70 eV and a strong broad orange light emission centered at 634 nm, with a full width at half maximum (FWHM) of 142 nm (0.44 eV). The emission has a long photoluminescence (PL) lifetime of 582 ns, while the intensity is constant over a very broad temperature range (145-415 K) with a photoluminescence quantum yield (PLQY) of at least 20.3% at RT. Above 415 K the material undergoes a structural phase transition from monoclinic (*C*2/*c*) to orthorhombic (*Ibam)* accompanied by a red shift in the bandgap and a quench in the photoluminescence emission. Density functional theory calculations support the trend in the optical properties and the 1D electronic nature of the structure, where the calculated carrier effective masses along the inorganic chain are significantly lower than those perpendicular to the chain. Thin films of the compound readily fabricated from solutions exhibit the same optical properties, but with improved PLQY of 36%,

for a 60 nm thick film, among the highest reported for lead-free low-dimensional 2D and 1D perovskites and metal halides.

INTRODUCTION

Halide perovskites are a unique family of semiconductors[1-2] that can be efficiently exploited in a wide range of applications spanning from solid state solar cells,[3-4] γ-ray detectors,[5] lasing,[6] thermography[7] and photocatalysis[8] to LEDs.[9-10] The vast majority of these materials have the perovskite structure which is defined as one featuring octahedral metal MX_6 centers where the octahedra connect to each other by sharing only corners to form 3D, 2D, and 1D structures. The 3D halide perovskites are formulated as AMX_3 ($A = CH_3NH_3^+$ (MA), $HC(NH_2)_2^+$ (FA), Cs^+; $M = Ge^{2+}$, Sn^{2+}, Pb^{2+}; $X = Cl^-$, Br^-, I^-).[11,12] $A'_2A_{n-1}M_nX_{3n+1}$ formula describes 2D perovskites, where A′ is a monovalent or divalent ($A'A_{n-1}M_nX_{3n+1}$) organic cation acting as a spacer between the perovskite layers and A is monovalent cation,[13-14] while 1D materials (e.g. $A'M_nX_{2n+1}$)[15-16] and often 0D nanostructures are referred to as perovskites (e.g. AMX_3 quantum dots). If the MX_6 octahedra, however, are not connected by sharing corners, the structures are not proper perovskites and can be referred to as perovskitoids.[17]

A relatively recent and most prominent property of this class of materials is their ability to chemically engineer and shape the light emission spectra (e.g. strong broad light and white light emission),[18-20] color stability, and color rendering capability, either as stand-alone semiconductor compounds in light emitting diodes (LEDs)[21] or in combination with a phosphor.[22] Hybrid halide perovskites also offer the advantage of solution processability,[23] fine tuning of optical properties,[24] high photoluminescence quantum yield (PLQY) and composition of earth abundant chemical elements,[25] thus lowering the cost and expanding the color gamut application range of the existing technologies.[26]

A plethora of hybrid perovskite and metal halide candidate materials with notable PLQY values have been reported towards this end: 2D compounds such as (EDBE)-[$PbBr_4$] (EDBE: 2,2′-(ethylenedioxy)bis(ethylammonium) with 9% PLQY,[27] (2,6- dmpz)$_3Pb_2Br_{10}$ (2,6-dmpz: 2,6-dimethylpiper-azine) with 12% PLQY,[28] 1D compounds such as (AD)Pb_2Cl_5 (AD: acridine) with 7.45% PLQY,[29] (AQ)$PbCl_4$ (AQ: 3-aminoquinoline) with 9% PLQY,[30] (TMEDA)Pb_2Br_6 (TMEDA: N,N,N'-trimethylethylene-diammonium) with 10% PLQY,[31] $(C_4N_2H_{14})PbBr_4$ and $(C_4N_2H_{14})Pb_{0.987}Mn_{0.013}Br_4$ ($C_4N_2H_{14}$: N, N-dimethylethylenediamine) with 20% and

28% PLQY respectively,[32-33] (TDMP)$PbBr_4$ (TDMP: trans-2,5-dimethylpiperazine) with 45% PLQY,[34] and 0D materials in single crystal form such as $(C_4N_2H_{14}Br)_4SnBr_3I_3$ with 85% PLQY,[35] and $(C_9NH_{20})_2SbCl_5$ with 95% PLQY.[36] In the latter two cases the achieved PLQY values are comparable to those recorded for $CsPbX_3$ (X: Br, I) perovskite quantum dots (QD),[37] which exhibit near-unity PLQY.[38-39] However perovskite QDs suffer from poor long-term stability that could limit their implementation in real life applications.[40-41]

Two fundamental prerequisites for the commercial utilization of a new material are their composition of non-toxic elements (e.g. Sn^{2+}) and their long-term environmental stability.[42] Most of the reported hybrid materials with highly efficient light emission are based on Pb^{2+}, and only few are stable under extreme conditions, such as $[Pb_2Cl_2]^{2+}[^-O_2C(CH_2)_4CO_2^-]$ which is water stable for 24h[43] and [N-methyldabconium]PbI_3 which is water stable for one month.[44]

Nonetheless, there is significant interest in developing less toxic lead-free compounds. Progress in this regard includes $(C_8NH_{12})_4Bi_{0.57}Sb_{0.43}Br_7 \cdot H_2O$ (4.5% PLQY),[45] $(PEA)_2SnI_4$ (PEA: phenylethylamine, 6.4% PLQY as nanodisks),[46] $(TEA)_2SnI_4$ (TEA: thienylethylamine, 18.8% PLQY as nanodisks),[47] $(C_{18}H_{35}NH_3)_2SnBr_4$ (88% PLQY as colloidal suspension),[48] $(C_5H_7N_2)_2ZnBr_4$ (19% PLQY)[49], $(Bmpip)_2SnI_4$ (Bmpip: 1-butyl-1-methyl-piperidinium, 35% PLQY),[50] $(C_4N_2H_{14}I)_4SnI_6$ (75% PLQY),[36] $Cs_3Cu_2I_5$ (90% PLQY)[51] and $(C_9NH_{20})_2SbCl_5$ (95% PLQY).[36] In the majority of cases these materials have molecular 0D structures. Even though they can be efficient light emitters, generally there is limited information on their environmental stability, or how they perform well above room temperature.

Addressing the above concerns, we report here the synthesis of 1D $(DAO)Sn_2I_6$ (DAO: 1,8-octyldiammonium) compound with a new structure, which is water stable for more than 15h, and exhibits strong broad orange light emission at room temperature (RT) with 20.3% PLQY. To our knowledge, this PLQY value is among the highest for low dimensional (1D, 2D) metal halide broad light emitters in single crystal form (Table S1). The PL is characterized by a constant PL linewidth in the 175-415 K temperature range and a stable PL intensity in the 145-415 K range. Power dependent PL studies suggest that the origin of the broad light emission is ascribed to trap states. Films of $(DAO)Sn_2I_6$ can be made using a one-step (OS) solution deposition method based on this material's precursor components. The films maintained the crystal's excellent optical properties, and achieve an enhanced bright broad light emission with at least 36%

PLQY.

RESULTS AND DISCCUSSION

Synthetic Aspects and Water Stability

High quality single crystals of $(DAO)Sn_2I_6$ were obtained by the reaction of an off-stoichiometric amount of $SnCl_2{\times}2H_2O$ and 1,8-diamino octane (2:0.5) in hydrogen iodide (HI) and hypophosphorous acid (H_3PO_2) solution (volume ratio 5:8). This specific reagent ratio was used for the acquisition of large yellow single crystals (~0.2 cm). When equimolar reactants ratio (1:1) for Sn and DAO was tested instead, powder size crystals were formed. The resulting $(DAO)Sn_2I_6$ crystals were filtered in air and dried under vacuum. The presence of high amount of H_3PO_2 in the solution helps to suppress Sn^{2+} oxidation and formation of orange SnI_4 crystals that can contaminate the final product. Notably, $(DAO)Sn_2I_6$ can remain in its mother liquor for months without formation of SnI_4.

Powder X-ray diffraction (PXRD) measurements verified the phase purity of the as made single crystals, as the calculated PXRD pattern from the single crystal structure refinement matched exactly the experimentally recorded one (Figure 1a, b). SEM studies revealed the uniform well faceted rectangular shape of the single crystals, see Figure 1c. Remarkably, the resulting $(DAO)Sn_2I_6$ crystals are stable not only after washing with water, but can also remain in liquid water for more than 15h without structural decomposition as determined by PXRD, Figure 1a, b. Given the well-known extreme moisture sensitivity of Sn^{2+} based perovskite materials, the water stability of $(DAO)Sn_2I_6$ is surprising. To illustrate this performance, we compared the stabilities of the most air stable Pb based perovskites, such as the highly "hollow" 3D $(MA)_{0.56}(en)_{0.44}(Pb)_{0.692}(I)_{2.824}$ (*en*: ethylenediammonium),[52] the 2D $(HA)_2(MA)_3Pb_4I_{13}$ (HA: hexylammonium) and also the pristine 3D $MAPbI_3$.[53] All these crystals decomposed immediately upon contact with water to yellow PbI_2, whereas the $(DAO)Sn_2I_6$ crystals remained intact for at least 15h (Figure 2). This exceptional water stability is accompanied by a diminished crystal solubility (at least three times lower) in common polar solvents such as dimethylformamide (DMF), dimethylacetamide (DMA), N-methyl-2-pyrrolidone (NMP) and dimethylsulfoxide (DMSO) as compared to higher dimensional hybrid halide perovskite analogues, such as 3D $MAPbI_3$[54] and 2D $(NH_3C_mH_{2m}NH_3)(CH_3NH_3)_{n-1}Pb_nI_{3n+1}$.[55]

X-Ray Photoelectron Spectroscopy (XPS) measurements performed on the samples before and after the water treatment indicated no valence changes (using SnI_2 and SnI_4 crystals as standards), (Figure S1). Furthermore, the UV-VIS optical absorption and Raman spectra of fresh crystals and crystals after water immersion were unchanged (Figure 3, S2a). After 2 weeks of air exposure XPS measurements detected surface oxidation of the Sn^{2+} into Sn^{4+} (Figure S1b) and crystal color change from yellow to brown and black. However, this is limited to the surface of the crystals and there is no underlying decomposition even after 90 days exposure in air, as concluded by PXRD measurements (Figure S3). Thermogravimetric analysis (TGA) measurements revealed that $(DAO)Sn_2I_6$ is thermally stable up to 558K, which is the same temperature range as the 2D Pb based Ruddlesden-Popper perovskites[53] and about 25 K lower than the 3D $MASnI_3$ perovskites (Figure S4b).[52] Differential scanning calorimetry (DSC) measurements followed by PXRD indicate the presence of a phase transition, expressed as an endothermic peak at 425K (Figure S4a). We therefore, investigated the crystal structure over a wide range of temperature to elucidate the distinguishing features of the phase changes and look for other phase transitions, as described below.

Structural properties

Single crystal XRD analysis revealed that the material crystallizes in the monoclinic centrosymmetric *C*2/*c* space group at room temperature. There is one crystallographically independent Sn^{2+} cation and four I^- ions which through the presence of an inversion centre and a glide plane generate a 1D inorganic chain along the crystallographic *c*-axis. The chain consists of corner sharing $[SnI_5]^{3-}$ moieties (Figure 4a). The Sn^{2+} cations are coordinated by five I^- ions and exhibit a distorted square pyramidal geometry. The structure consists of an unprecedented 1D double inorganic chain based on corner sharing square pyramidal $[SnI_5]^{3-}$ moieties, which are separated and charge balanced by 1,8-octyldiammonium cations. Each square pyramidal moiety is connected by the equatorial iodide atoms to four other $[SnI_5]^{3-}$ units at an angle (Sn-I(4)-Sn) of 114.638(11)° creating in this way a 1D double inorganic ladder-like chain of opposite facing pyramids (Figure 4b). This geometry indicates that the $5s^2$ lone pair in the Sn^{2+} ions is stereochemically active with its expected location being on the opposite side of the axial Sn-I bonds. In the square pyramidal $[SnI_5]^{3-}$

moiety the axial Sn-I(3) distance is 2.8948(3) Å while the equatorial distances range from 3.0890(3) Å to 3.3116(3) Å, for Sn-I(4) and Sn-I(2) respectively.

Among the inorganic chains, propagating along the crystallographic *c*-axis reside two opposite phasing, double protonated organic (DAO) molecules charge balancing the structure. The linkers are staggered along the axis direction, while the terminal ammonium groups on the alternating organic molecules are pointing along the *b*-axis towards opposite chains. The planes of the linkers are separated by 2.5 Å, while the distance among the N-H hydrogens and the bridging equatorial I(2) anions of the $[SnI_5]^{3-}$ pyramids is 2.87 Å, signalling moderate hydrogen bond interactions (Figure S6).[56]

Phase transition. The $(DAO)Sn_2I_6$ exhibits a temperature dependent phase transition from monoclinic to orthorhombic as determined by PXRD and single crystal XRD studies. Scanning the range of 80K to 500K we observed one clear phase transition between 410K-440K and verified the compound is stable up to at least 500K. From 80K to 410K there is a shift of the PXRD pattern to lower 2θ values, indicative of lattice thermal expansion. The solved and refined single crystal structure at 100K was found to be the same as the RT one (Table 1). From 410K to 500K, however, a structural phase transformation is evidenced by the disappearance of the (111) diffraction peak of the monoclinic phase and the appearance of the (121) peak of the orthorhombic phase (Figure S5). When the temperature reaches 440K the structure increases in symmetry, adopting the orthorhombic centrosymmetric *Ibam* space group, based on single crystal XRD measurements (Figure 5, Table 1). This phase transition is accompanied by a change in color from yellow to dark red and a gradual increase in the unit cell volume from 2369.30(15) $Å^3$ to 2476.9(2) $Å^3$ representing a ~4.5% expansion (Table 1). This large expansion is coupled to the relaxation of the structure, as the inorganic chain becomes less distorted at high temperature (HT), as evidenced by the opposite equatorial Sn-I(1)-Sn and Sn-I(4)-Sn angles changing from 101.108(8)° and 114.638(11)° at room temperature (RT), to 98.94(3)° and 139.38(5)° at HT respectively. The asymmetry of the distorted $[SnI_5]^{3-}$ pyramid at RT as compared to the less distorted HT phase, is also clear by the change in the equatorial Sn-I bond lengths. In the RT phase they reside at distances of Sn-I(4), Sn-I(1) and Sn-I(2) 3.0890(3) Å, 3.2896(3) Å and 3.3116(3) Å respectively, while at HT, the corresponding values are 3.1783(7) Å and 3.2050(8) Å, for Sn-I(2) and Sn-I(3) respectively. These parameters

clearly depict the higher distortion of the pyramids of the RT phase, which have a direct effect on the optical properties, as there is crystal colour change from yellow to red.

The organic cations at HT are also relaxed, shifting from the bent RT configuration, to an almost linear one, stretching across two neighboring inorganic chains. The corresponding distance among the N-H hydrogens and the axial I(1) anions of the $[SnI_5]^{3-}$ pyramids is 2.93 Å. This is a significant difference between the HT and RT structures, as in the first case the two ammonium groups are facing the same inorganic chain, whereas at HT, the two ammonium groups charge balance opposite inorganic chains across the *a*-axis (Figure S7). In this case the ammonium groups lay closer to the axial iodide ions and not to the equatorial as it observed in the RT phase.

Electronic structure calculations

Density functional theory (DFT) calculations provide insight about the electronic structure and the semiconductor properties of $(DAO)Sn_2I_6$ at room temperature (298 K, *C*2/*c*) and high temperature (440 K, *Ibam)*. The electronic band structure at RT, exhibits bands with strong energy dispersion in the $[Sn_2I_6]$ chain direction and low dispersions in perpendicular directions, reflecting the 1D character of the crystals (Figure 6). The conduction band minimum (CBM) is located at the Γ point of the Brillouin zone (BZ), while the valence band maximum (VBM) is found, at the edge of BZ (M point) giving rise to an indirect bandgap of 2.215 eV. The computed band gap is a little bit lower than the experimental determined one at 2.70 eV, which is expected from the chosen level of theory (see Supporting Information). The valence band maximum (VBM) consists mostly of I(5p) orbitals with a contribution from Sn(5s) lone pair states, while CBM consists mostly of Sn(5p) orbitals (Figure S8a, S10a). For the less distorted HT phase, the band gap remains indirect in nature, the CBM being located at the X point of the BZ, and the VBM at the G_0 point, exhibiting again an indirect bandgap of 2.149 eV at this level of computation. The calculations therefore do predict a red shift of the band gap consistently with crystal color change from yellow to red for the HT phase (Figure 6b). Partial densities of states do not exhibit strong difference between the two phases (Figure S8). The main contrast is found in the contributions of the outer (I_{out}, axial) and inner (I_{in}, equatorial) iodide atoms of the inorganic chain to the VBM and CBM at both temperatures (Figure S9). At RT the I_{out} peak is shifted in comparison to the I_{in} peak, indicating more localized states, while at HT the contributions of I_{in} and I_{out} exhibit a better overlap. This could be ascribed to the

stronger interaction of the axial iodide atoms with the ammonium groups at RT, through moderate hydrogen bonding. The distance among the N-H hydrogens and the bridging equatorial I(2) anions of the $[SnI_5]^{3-}$ pyramids is 2.87 Å at RT (see above) while at HT it shifts to 3.50 Å, signalling weaker interaction.

An important parameter for the evaluation of the charge transport properties in a semiconductor material, is the carrier effective masses.[57] In $(DAO)Sn_2I_6$ due to the reduced dimensionality of the framework, we calculated these parameters along the inorganic chain and perpendicular to the chain. For the RT phase, the values are $m_{e,//}^* = 0.32m_0$ and $m_{h,//}^* = 0.72m_0$ for electrons and holes respectively along the 1D inorganic chain, while these values exhibit a strong anisotropy perpendicular to the chain, $m_{e,\perp}^* = 2.72m_0$ and $m_{h,\perp}^* = 2.86m_0$. These results clearly suggest that there is negligible electronic coupling between neighbouring inorganic chains. The effective masses of 1D $(DAO)Sn_2I_6$ $m_e^*$and m_h^* along the inorganic chain are slightly larger than those reported for the 3D $MASnI_3$ and 2D $(BA)SnI_4$ (BA: butylammonium) compounds, $m_e^* = 0.13m_0$, $m_h^* = 0.28m_0$[58] and $m_e^* = 0.13m_0$, $m_h^* = 0.15m_0$[59] respectively.

For the HT phase, DFT calculations yield lower masses $m_{e,//}^* = 0.09m_0$, $m_{h,//}^* = 0.33m_0$ and $m_{e,\perp}^* = 1.18m_0$, $m_{h,\perp}^* = 6.23m_0$ along the 1D inorganic chain and perpendicular to the chain respectively. This significant difference between the two phases is clearly connected to the much less distorted nature of the HT phase, where the increased Sn-I orbital overlap leads to broader bands and better charge transport properties. This trend was also observed for the 3D $MAPbI_3$ analogs, where lowering of the crystal symmetry from the cubic undistorted phase to the distorted tetragonal phase, lead to a reduction of the Pb-I orbital overlap and higher carrier effective masses.[60]

Optical absorption and photoluminescence

UV-VIS absorption spectra of $(DAO)Sn_2I_6$ reveal a sharp absorption edge at 2.70 eV for both the pristine and the water treated sample (Figure 3, S2a). The RT Raman spectra of the fresh and water treated sample were also identical (Figure S2b). The spectra are dominated by sharp vibrational peaks, which are characteristic of low-dimensional non-perovskite metal halide materials,[28] in contrast to the broad spectral features that are observed for 3D perovskites.[61] Comparing the spectra for $(DAO)Sn_2I_6$ to those of the 1D compound $(CH_3)_3SSnI_3$, we can ascribe the peaks at lower

wavenumbers (15-100 cm^{-1}) to the bending of the I−Sn−I bonds, whereas the peaks at higher wavenumbers (100-200 cm^{-1}) derive from the stretching of the Sn−I bonds.[62-63] Notably the vibration peaks of $(DAO)Sn_2I_6$ at RT, are much sharper than those of $(CH_3)_3SSnI_3$, depicting the higher rigidity of the $(DAO)Sn_2I_6$ structure.

Upon excitation of the as made crystals with a 400 nm beam $(DAO)Sn_2I_6$ exhibits a broad strong emission centered at 634 nm with a large full width at half maximum (FWHM) of 142 nm (0.44 eV). The PL maximum has a large energy shift of 174 nm (0.75 eV) (Figure 7a). This behavior is typical for broad light emitter materials,[64] however, its origin depends on a number of structural parameters (dimensionality,[65] composition,[66] presence of defects[67]), and is unique for each compound.[68-69] The strong broad light emission of $(DAO)Sn_2I_6$ gave a PLQY of 20.3% (Figure S11), while the PL peak position and FWHM is the same regardless of excitation power (Figure S12). This PLQY value is the among the highest recorded for 1D metal halides, and a record value for lead free 1D broad light emitter materials in single crystal form.[70]

The corresponding CIE (International Commission on Illumination) chromaticity coordinates are (0.55, 0.42), with a much larger contribution from the red region of the spectrum as compared to pure white light, which has chromaticity coordinates of (0.33, 0.33). This gives the emission from $(DAO)Sn_2I_6$ a correlated color temperature (CCT) of 1822 K (warm orange light), and a color-rendering index (CRI) value of 75, meaning that this material is suitable for outdoor lighting (Figure 8b). CIE coordinates and CCT values were calculated using the ColorCalculator by OSRAM Sylvania, Inc. CRI index quantifies how accurately illuminated colors are reproduced; for indoor lighting values above 80 are required.[71]

Photoemission yield spectroscopy in air (PYSA) measurements provided insight into the electronic band alignment of the synthesized perovskite materials.[72] The position of the valence band maxima (VBM) was determined through PYSA measurements, while the conduction band minima (CBM) was determined by subtracting the corresponding optical band gap values from the measured VBM energies. The recorded values for the pristine crystals, the water treated ones as well as the 3D $MASnI_3$ are presented in Figure S13. The VBM of the pristine material lays a little deeper in energy than the water treated one, which could be an indication of the surface degradation of the water treated sample. Furthermore, the fact that the pristine material has higher ionization energy than $MASnI_3$, is consistent with the higher air

stability of (DAO)Sn_2I_6, considering that $MASnI_3$ is stable in air for a few minutes only.[73]

Origin of PL emission

In order to verify whether the emission is a bulk property and does not originate from surface defects, the large single crystals were grounded and the PL spectra were recorded, showing no difference in PL intensity (Figure S14), suggesting that the PL is indeed a bulk property. To gain insight into the mechanism of the broad emission, variable-temperature PL measurements were performed from 5 to 295K. With decreasing temperature there is a small gradual red shift of the PL peak from 631 nm (295K) position to 655 nm (145K), while at 115K a big red shift to 745 nm is observed (Figure 7b). This could be ascribed to an unidentified phase transition close/below 100K (Figure 5). The FWHM of the peaks gradually shrinks, from 142 nm to 135 nm from 295K to 175K (Figure S15b). Below this temperature the PL emission becomes significantly broader, exhibiting FWHM values ranging from 198 to180 nm, for 145K to 5K respectively (Figure S15b).

The measured average decay lifetime at RT is 582 ns using multi-exponential fitting of the emission decay curve (Figure 7c), showing three components with decay constants of 0.7, 187 and 935 ns. At 77 K the lifetime shows a single exponential decay with decay constant of 968 ns, comparable with the long decay component at RT (Table S14). The magnitude of the PL lifetime in (DAO)Sn_2I_6 may be ascribed to a trap assisted emission mechanism (see below).[74] Notably, at RT the recorded lifetime is much longer than those in QDs (Quantum dots) materials, with values of few ns,[38] 1D strong light emitting metal halide materials, such as $C_4N_2H_{14}PbBr_4$ with recorded values of few tens of ns,[32] $C_5H_{16}N_2Pb_2Br_6$ with a lifetime of about one hundred ns,[31] and 1D fully inorganic white light emitters such as $CsCu_2I_3$, with values below one hundred ns.[75]

We also measured the dependence of PL intensity as a function of excitation power density and found that it does not follow a linear trend (for various temperatures), as it saturates at high power flux. This suggests that the source of emission stems from permanent defects and not self-trapped excitons (STEs) (Figure 7d).[76-77] Correcting the PL spectra by the excitation intensity, we observe that the PL quenches at higher excitation power (Figure S16), which is a typical behavior for radiative trap-assisted recombination.[74, 78-79] In the latter case, emission is observed when a photogenerated

charge is trapped in a midgap state and combines with a counter charge before it relaxes back to the ground state via a nonradiative pathway.[80]

To evaluate the robustness of the PL emission at higher temperatures, variable temperature measurements were carried out up to 575 K (high temperature range) (Figure S17). Remarkably, the $(DAO)Sn_2I_6$ emission exhibits not only a constant PL linewidth in the temperature range of 175-415 K but a sustainable PL intensity over the broad range of 145-415 K (Figure S15a). Interestingly, above 415K the PL quenches (Figure S17). This is in accordance with the recorded phase transition (Figure S5) from the distorted monoclinic phase (*C*2/*c*) at 410 K, to the less distorted orthorhombic phase (*Ibam*) at 440 K (Figure 5). It is possible that under this structural configuration, and heat treatment of the material, any emitting defect is suppressed or changed in character. Similarly, although the structural and electronic properties are unaffected by the water treatment (based on PXRD, UV-VIS and Raman measurements), the PL emission is quenched. This is in alignment with the assignment of PL to permanent defects that can be modified without perturbing the bulk material's properties.

The PL emission spectra are intact, both in terms of emission wavelength and shape until the temperature of the phase transition is reached (Figure S18). The PL stability within the RT phase limit is further supported by the determined CIE chromaticity coordinates of (0.53, 0.45) at 415 K, and the color-rendering index (CRI) value of 73, which are very close to the RT recorded values of (0.55, 0.42) and 75 respectively, verifying the excellent high temperature emission performance of the material. This finding is important because an LED operating temperature can be as high as 425K.[81-82]

Film deposition

A highly attractive feature of $(DAO)Sn_2I_6$ is its ability to deposit uniform high-quality thin films. Because of the moderate solubility (see above) of the crystals in a variety of polar solvents, we used precursor salts instead. Freshly prepared octylenediammonium diodide ($DAO\text{-}I_2$) (see S.I.) and SnI_2 were dissolved in DMF, in an off stoichiometric ratio ($DAO\text{-}I_2$: SnI_2 = 1:1), and spin coated, using a one-step (OS) deposition method (see S.I.) giving rise to a colorless film which upon UV illumination exhibited strong orange light emission (Figure 8c). If a stoichiometric ratio ($DAO\text{-}I_2$: SnI_2 = 1:2) is used instead, a red film is formed, which can be ascribed to the formation of the 2D Ruddlesden-Popper $(DAO)SnI_4$ compound. This can be verified by

comparing the PXRD patterns of the reported Pb analogue $(DAO)PbI_4$[55] and the corresponding film (Figure S19).

Atomic force microscopy (AFM) measurements revealed that a uniform, 60 nm thin film was formed, with a surface roughness RMS value of 9.8 nm (Figure S20). PXRD measurements shed light on the film composition, which consists of an (110) oriented $(DAO)Sn_2I_6$ major crystalline phase (Figure S21). There is also a small diffraction peak present at 6.6° 2θ, which is not predicted from the calculated pattern, nor from unreacted precursor species (Figure S22) and may be an indication of the formation of a different minor phase. Nonetheless, the film's optical absorption, emission and the PLE spectra (Figures 9, S23-24) are very similar to those of the single crystals. This verifies that the origin of the PL emission is the same in both the film and the crystals. The thin films, however, exhibited a much improved PLQY of 36% (Table 2). The enhanced PLQY value is further supported by the significantly longer PL decay average lifetime at RT which was determined to be 1114 ns by multi-exponential fitting (Figure S25). The decay components are similar to those of the crystals but with much larger portion of the photons emitted from the longer decay route (see table S14), similar to the dynamics at 77K. The slower decay seems to indicate a more efficient transfer of the excitons to the lower energy states. Furthermore, the corresponding CIE chromaticity coordinates of (0.59, 0.40) (Figure 8d), are very close to the bulk crystals recorded ones of (0.55, 0.42), while the calculated color-rendering index (CRI) value is 74, rendering this film a competent light emitter as the single crystals (CRI value 75). PYSA measurements demonstrated the corresponding CBM and VBM energy levels with values of 2.73(5) eV and 5.43(5) eV respectively. These results lay the path for the further optimization of film assembly and PL performance for future device explorations.

CONCLUSIONS

The new 1D Sn based metal halide compound $(DAO)Sn_2I_6$ is stable in contact with water for 15h, posing as a record stability for a Sn(II) based metal halide material, while exhibiting highly efficient broad light emission with PLQY of 20.3%, in single crystal form. Equally important is that the material maintains this emission performance over a wide temperature range, and up to 415 K, surpassing the operating temperature of an LED. Furthermore, at RT the PL lifetime is very long (582 ns) thus allowing for efficient carrier recombination. Thin films can be fabricated exhibiting the same

emission properties (CRI values and CIE coordinates) as the bulk crystals but with an improved PLQY value of 36%, for a 60 nm thick film. The origin of the strong emission is ascribed to the existence of permanent defects. The (DAO)Sn_2I_6 stands out not only as an auspicious environmentally friendly and stable potential LED semiconductor candidate, but also as a photocatalyst, based on its high PL lifetime values and water stability. These results demonstrate the versatile nature of perovskitoid hybrid halide materials, laying the path for the design of next generation of water stable lead-free semiconductors.

ASSOCIATED CONTENT

Supporting Information

Materials and methods, synthetic details, additional supplementary figures and tables about material characterization, X-ray diffraction measurements, photoluminescence measurements, XPS measurements, AFM measurements, thermogravimetric analysis and PYSA measurements.

This material is available free of charge via the Internet at http://pubs.acs.org.

X-ray crystallographic data for (DAO)Sn_2I_6-100K

X-ray crystallographic data for (DAO)Sn_2I_6-293K

X-ray crystallographic data for (DAO)Sn_2I_6-440K

AUTHOR INFORMATION

Corresponding Authors

m-kanatzidis@northwestern.edu

Present address

[#]Department of Chemical and Environmental Engineering, Yale University, 9 Hillhouse Avenue, New Haven, CT 06520, USA

Notes

The authors declare no competing financial interest.

ACKNOWLEDGMENT

This work is primarily supported by the Department of Energy, Office of Science, Basic Energy Sciences, under Grant No. SC0012541 (sample synthesis, structure and property characterization). This work made use of the SPID, and EPIC facilities of Northwestern University's NU*ANCE* Center, as well as the IMSERC facilities, which have received support from the Soft and Hybrid Nanotechnology Experimental (SHyNE) Resource (NSF ECCS-1542205); the MRSEC program (NSF DMR-1720139) at the Materials Research Center, from the State of Illinois, and the International Institute for Nanotechnology (IIN). J.E. acknowledges Institut Universitaire de France for funding. This project has received funding from the European Union's Horizon 2020 research and innovation Program under the grant agreement No 862656. This work was granted access to the HPC resources of [TGCC/CINES/IDRIS] under the allocation 2019-A0070907682 made by GENCI. This work was performed, in part, at the Center for Nanoscale Materials, a U.S. Department of Energy Office of Science User Facility, and supported by the U.S. Department of Energy, Office of Science, under Contract No. DE-AC02-06CH11357. Work on the thin film fabrication and evaluation at Rice was supported by start-up funds under the molecular nanotechnology initiative and also the DOE-EERE 2022-1652 program.

REFERENCES

1. Stoumpos, C. C.; Kanatzidis, M. G., The Renaissance of Halide Perovskites and Their Evolution as Emerging Semiconductors, *Acc. Chem. Res.* **2015,** *48*, 2791-2802.
2. Stoumpos, C. C.; Kanatzidis, M. G., Halide Perovskites: Poor Man's High-Performance Semiconductors, *Adv. Mater.* **2016,** *28*, 5778-5793.
3. Jeon, N. J.; Noh, J. H.; Yang, W. S.; Kim, Y. C.; Ryu, S.; Seo, J.; Seok, S. I., Compositional engineering of perovskite materials for high-performance solar cells, *Nature* **2015,** *517*, 476.
4. Tsai, H.; Nie, W.; Blancon, J.-C.; Stoumpos, C. C.; Asadpour, R.; Harutyunyan, B.; Neukirch, A. J.; Verduzco, R.; Crochet, J. J.; Tretiak, S.; Pedesseau, L.; Even, J.; Alam, M. A.; Gupta, G.; Lou, J.; Ajayan, P. M.; Bedzyk, M. J.; Kanatzidis, M. G.; Mohite, A. D., High-efficiency two-dimensional Ruddlesden–Popper perovskite solar cells, *Nature* **2016,** *536*, 312.
5. He, Y.; Ke, W.; Alexander, G. C. B.; McCall, K. M.; Chica, D. G.; Liu, Z.; Hadar, I.; Stoumpos, C. C.; Wessels, B. W.; Kanatzidis, M. G., Resolving the Energy of γ-Ray Photons with MAPbI3 Single Crystals, *ACS Photonics* **2018,** *5*, 4132-4138.
6. Zhu, H.; Fu, Y.; Meng, F.; Wu, X.; Gong, Z.; Ding, Q.; Gustafsson, M. V.; Trinh, M. T.; Jin, S.; Zhu, X. Y., Lead halide perovskite nanowire lasers with low lasing thresholds and high quality factors, *Nature Mater.* **2015,** *14*, 636.
7. Yakunin, S.; Benin, B. M.; Shynkarenko, Y.; Nazarenko, O.; Bodnarchuk, M. I.; Dirin, D. N.; Hofer, C.; Cattaneo, S.; Kovalenko, M. V., High-resolution remote thermometry and thermography using

luminescent low-dimensional tin-halide perovskites, *Nature Mater.* **2019,** *18*, 846-852.
8. Hong, Z.; Chong, W. K.; Ng, A. Y. R.; Li, M.; Ganguly, R.; Sum, T. C.; Soo, H. S., Hydrophobic Metal Halide Perovskites for Visible-Light Photoredox C−C Bond Cleavage and Dehydrogenation Catalysis, *Angew. Chem. Int. Ed.* **2019,** *58*, 3456-3460.
9. Zhang, L.; Yang, X.; Jiang, Q.; Wang, P.; Yin, Z.; Zhang, X.; Tan, H.; Yang, Y.; Wei, M.; Sutherland, B. R.; Sargent, E. H.; You, J., Ultra-bright and highly efficient inorganic based perovskite light-emitting diodes, *Nat. Commun.* **2017,** *8*, 15640.
10. Luo, C.; Li, W.; Fu, J.; Yang, W., Constructing Gradient Energy Levels to Promote Exciton Energy Transfer for Photoluminescence Controllability of All-Inorganic Perovskites and Application in Single-Component WLEDs, *Chem. Mater.* **2019,** *31*, 5616-5624.
11. Koji, Y.; Hiroshi, K.; Takashi, M.; Tsutomu, O.; Sumio, I., Structural Phase Transition and Electrical Conductivity of the Perovskite CH3NH3Sn1-xPbxBr3 and CsSnBr3, *Bull. Chem. Soc. Jpn.* **1990,** *63*, 2521-2525.
12. Stoumpos, C. C.; Malliakas, C. D.; Kanatzidis, M. G., Semiconducting Tin and Lead Iodide Perovskites with Organic Cations: Phase Transitions, High Mobilities, and Near-Infrared Photoluminescent Properties, *Inorg. Chem.* **2013,** *52*, 9019-9038.
13. Mitzi, D. B., Templating and structural engineering in organic–inorganic perovskites, *J. Chem. Soc., Dalton Trans.* **2001**, 1-12.
14. Stoumpos, C. C.; Cao, D. H.; Clark, D. J.; Young, J.; Rondinelli, J. M.; Jang, J. I.; Hupp, J. T.; Kanatzidis, M. G., Ruddlesden–Popper Hybrid Lead Iodide Perovskite 2D Homologous Semiconductors, *Chem. Mater.* **2016,** *28*, 2852-2867.
15. Peng, Y.; Yao, Y.; Li, L.; Wu, Z.; Wang, S.; Luo, J., White-light emission in a chiral one-dimensional organic–inorganic hybrid perovskite, *J. Mater. Chem. C* **2018,** *6*, 6033-6037.
16. Gao, L.; Spanopoulos, I.; Ke, W.; Huang, S.; Hadar, I.; Chen, L.; Li, X.; Yang, G.; Kanatzidis, M. G., Improved Environmental Stability and Solar Cell Efficiency of (MA,FA)PbI3 Perovskite Using a Wide-Band-Gap 1D Thiazolium Lead Iodide Capping Layer Strategy, *ACS Energy Letters* **2019,** *4*, 1763-1769.
17. Stoumpos, C. C.; Mao, L.; Malliakas, C. D.; Kanatzidis, M. G., Structure–Band Gap Relationships in Hexagonal Polytypes and Low-Dimensional Structures of Hybrid Tin Iodide Perovskites, *Inorg. Chem.* **2017,** *56*, 56-73.
18. Febriansyah, B.; Giovanni, D.; Ramesh, S.; Koh, T. M.; Li, Y.; Sum, T. C.; Mathews, N.; England, J., Inducing formation of a corrugated, white-light emitting 2D lead-bromide perovskite via subtle changes in templating cation, *J. Mater. Chem. C* **2020,** *8*, 889-893.
19. Ji, C.; Wang, S.; Li, L.; Sun, Z.; Hong, M.; Luo, J., The First 2D Hybrid Perovskite Ferroelectric Showing Broadband White-Light Emission with High Color Rendering Index, *Adv. Funct. Mater.* **2019,** *29*, 1805038.
20. Nagami, A.; Okamura, K.; Ishihara, T., Optical properties of a quantum wire crystal, C5H10NH2PbI3, *Physica B: Condensed Matter* **1996,** *227*, 346-348.
21. Cho, H.; Jeong, S.-H.; Park, M.-H.; Kim, Y.-H.; Wolf, C.; Lee, C.-L.; Heo, J. H.; Sadhanala, A.; Myoung, N.; Yoo, S.; Im, S. H.; Friend, R. H.; Lee, T.-W., Overcoming the electroluminescence efficiency limitations of perovskite light-emitting diodes, *Science* **2015,** *350*, 1222-1225.
22. Zhou, J.; Huang, F.; Lin, H.; Lin, Z.; Xu, J.; Wang, Y., Inorganic halide perovskite quantum dot modified YAG-based white LEDs with superior performance, *J. Mater. Chem. C* **2016,** *4*, 7601-7606.
23. Wang, P.; Wu, Y.; Cai, B.; Ma, Q.; Zheng, X.; Zhang, W.-H., Solution-Processable Perovskite Solar Cells toward Commercialization: Progress and Challenges, *Adv. Funct. Mater.* **2019,** *29*, 1807661.
24. Yoon, H. C.; Kang, H.; Lee, S.; Oh, J. H.; Yang, H.; Do, Y. R., Study of Perovskite QD Down-Converted LEDs and Six-Color White LEDs for Future Displays with Excellent Color Performance, *ACS Applied Materials & Interfaces* **2016,** *8*, 18189-18200.
25. Zhao, X.; Ng, J. D. A.; Friend, R. H.; Tan, Z.-K., Opportunities and Challenges in Perovskite Light-Emitting Devices, *ACS Photonics* **2018,** *5*, 3866-3875.
26. Zhang, R.; Lin, H.; Yu, Y.; Chen, D.; Xu, J.; Wang, Y., A new-generation color converter for high-power white LED: transparent Ce3+:YAG phosphor-in-glass, *Laser & Photonics Reviews* **2014,** *8*, 158-164.
27. Dohner, E. R.; Jaffe, A.; Bradshaw, L. R.; Karunadasa, H. I., Intrinsic White-Light Emission from Layered Hybrid Perovskites, *J. Am. Chem. Soc.* **2014,** *136*, 13154-13157.
28. Mao, L.; Guo, P.; Kepenekian, M.; Hadar, I.; Katan, C.; Even, J.; Schaller, R. D.; Stoumpos, C. C.; Kanatzidis, M. G., Structural Diversity in White-Light-Emitting Hybrid Lead Bromide Perovskites, *J. Am. Chem. Soc.* **2018,** *140*, 13078-13088.

29. Yang, X.; Ma, L.-F.; Yan, D., Facile synthesis of 1D organic–inorganic perovskite micro-belts with high water stability for sensing and photonic applications, *Chemical Science* **2019,** *10*, 4567-4572.
30. Barkaoui, H.; Abid, H.; Yangui, A.; Triki, S.; Boukheddaden, K.; Abid, Y., Yellowish White-Light Emission Involving Resonant Energy Transfer in a New One-Dimensional Hybrid Material: (C9H10N2)PbCl4, *The Journal of Physical Chemistry C* **2018,** *122*, 24253-24261.
31. Lin, H.; Zhou, C.; Neu, J.; Zhou, Y.; Han, D.; Chen, S.; Worku, M.; Chaaban, M.; Lee, S.; Berkwits, E.; Siegrist, T.; Du, M. H.; Ma, B., Bulk Assembly of Corrugated 1D Metal Halides with Broadband Yellow Emission, *Adv. Optical Mater.* **2019,** *7*, 1801474.
32. Yuan, Z.; Zhou, C.; Tian, Y.; Shu, Y.; Messier, J.; Wang, J. C.; van de Burgt, L. J.; Kountouriotis, K.; Xin, Y.; Holt, E.; Schanze, K.; Clark, R.; Siegrist, T.; Ma, B., One-dimensional organic lead halide perovskites with efficient bluish white-light emission, *Nat. Commun.* **2017,** *8*, 14051.
33. Zhou, C.; Tian, Y.; Khabou, O.; Worku, M.; Zhou, Y.; Hurley, J.; Lin, H.; Ma, B., Manganese-Doped One-Dimensional Organic Lead Bromide Perovskites with Bright White Emissions, *ACS Applied Materials & Interfaces* **2017,** *9*, 40446-40451.
34. Gautier, R.; Massuyeau, F.; Galnon, G.; Paris, M., Lead Halide Post-Perovskite-Type Chains for High-Efficiency White-Light Emission, *Adv. Mater.* **2019,** *31*, 1807383.
35. Zhou, C.; Tian, Y.; Yuan, Z.; Lin, H.; Chen, B.; Clark, R.; Dilbeck, T.; Zhou, Y.; Hurley, J.; Neu, J.; Besara, T.; Siegrist, T.; Djurovich, P.; Ma, B., Highly Efficient Broadband Yellow Phosphor Based on Zero-Dimensional Tin Mixed-Halide Perovskite, *ACS Applied Materials & Interfaces* **2017,** *9*, 44579-44583.
36. Zhou, C.; Lin, H.; Tian, Y.; Yuan, Z.; Clark, R.; Chen, B.; van de Burgt, L. J.; Wang, J. C.; Zhou, Y.; Hanson, K.; Meisner, Q. J.; Neu, J.; Besara, T.; Siegrist, T.; Lambers, E.; Djurovich, P.; Ma, B., Luminescent zero-dimensional organic metal halide hybrids with near-unity quantum efficiency, *Chemical Science* **2018,** *9*, 586-593.
37. Protesescu, L.; Yakunin, S.; Bodnarchuk, M. I.; Krieg, F.; Caputo, R.; Hendon, C. H.; Yang, R. X.; Walsh, A.; Kovalenko, M. V., Nanocrystals of Cesium Lead Halide Perovskites (CsPbX3, X = Cl, Br, and I): Novel Optoelectronic Materials Showing Bright Emission with Wide Color Gamut, *Nano Lett.* **2015,** *15*, 3692-3696.
38. Li, X.; Wu, Y.; Zhang, S.; Cai, B.; Gu, Y.; Song, J.; Zeng, H., CsPbX3 Quantum Dots for Lighting and Displays: Room-Temperature Synthesis, Photoluminescence Superiorities, Underlying Origins and White Light-Emitting Diodes, *Adv. Funct. Mater.* **2016,** *26*, 2435-2445.
39. Koscher, B. A.; Swabeck, J. K.; Bronstein, N. D.; Alivisatos, A. P., Essentially Trap-Free CsPbBr3 Colloidal Nanocrystals by Postsynthetic Thiocyanate Surface Treatment, *J. Am. Chem. Soc.* **2017,** *139*, 6566-6569.
40. Lu, C.; Li, H.; Kolodziejski, K.; Dun, C.; Huang, W.; Carroll, D.; Geyer, S. M., Enhanced stabilization of inorganic cesium lead triiodide (CsPbI3) perovskite quantum dots with tri-octylphosphine, *Nano Research* **2018,** *11*, 762-768.
41. Akkerman, Q. A.; D'Innocenzo, V.; Accornero, S.; Scarpellini, A.; Petrozza, A.; Prato, M.; Manna, L., Tuning the Optical Properties of Cesium Lead Halide Perovskite Nanocrystals by Anion Exchange Reactions, *J. Am. Chem. Soc.* **2015,** *137*, 10276-10281.
42. Snaith, H. J., Present status and future prospects of perovskite photovoltaics, *Nature Mater.* **2018,** *17*, 372-376.
43. Zhuang, Z.; Peng, C.; Zhang, G.; Yang, H.; Yin, J.; Fei, H., Intrinsic Broadband White-Light Emission from Ultrastable, Cationic Lead Halide Layered Materials, *Angew. Chem. Int. Ed.* **2017,** *56*, 14411-14416.
44. Xue, C.; Yao, Z.-Y.; Zhang, J.; Liu, W.-L.; Liu, J.-L.; Ren, X.-M., Extra thermo- and water-stable one-dimensional organic–inorganic hybrid perovskite [N-methyldabconium]PbI3 showing switchable dielectric behaviour, conductivity and bright yellow-green emission, *Chem. Commun.* **2018,** *54*, 4321-4324.
45. Zhang, R.; Mao, X.; Yang, Y.; Yang, S.; Zhao, W.; Wumaier, T.; Wei, D.; Deng, W.; Han, K., Air-Stable, Lead-Free Zero-Dimensional Mixed Bismuth-Antimony Perovskite Single Crystals with Ultra-broadband Emission, *Angew. Chem. Int. Ed.* **2019,** *58*, 2725-2729.
46. Chen, M. Y.; Lin, J. T.; Hsu, C. S.; Chang, C. K.; Chiu, C. W.; Chen, H. M.; Chou, P. T., Strongly Coupled Tin-Halide Perovskites to Modulate Light Emission: Tunable 550–640 nm Light Emission (FWHM 36–80 nm) with a Quantum Yield of up to 6.4%, *Adv. Mater.* **2018,** *30*, 1706592.
47. Lin, J.-T.; Liao, C.-C.; Hsu, C.-S.; Chen, D.-G.; Chen, H.-M.; Tsai, M.-K.; Chou, P.-T.; Chiu, C.-W., Harnessing Dielectric Confinement on Tin Perovskites to Achieve Emission Quantum Yield up to 21%, *J. Am. Chem. Soc.* **2019,** *141*, 10324-10330.

48. Zhang, X.; Wang, C.; Zhang, Y.; Zhang, X.; Wang, S.; Lu, M.; Cui, H.; Kershaw, S. V.; Yu, W. W.; Rogach, A. L., Bright Orange Electroluminescence from Lead-Free Two-Dimensional Perovskites, *ACS Energy Letters* **2019,** *4*, 242-248.
49. Yangui, A.; Roccanova, R.; McWhorter, T. M.; Wu, Y.; Du, M.-H.; Saparov, B., Hybrid Organic–Inorganic Halides (C5H7N2)2MBr4 (M = Hg, Zn) with High Color Rendering Index and High-Efficiency White-Light Emission, *Chem. Mater.* **2019,** *31*, 2983-2991.
50. Morad, V.; Shynkarenko, Y.; Yakunin, S.; Brumberg, A.; Schaller, R. D.; Kovalenko, M. V., Disphenoidal Zero-Dimensional Lead, Tin, and Germanium Halides: Highly Emissive Singlet and Triplet Self-Trapped Excitons and X-ray Scintillation, *J. Am. Chem. Soc.* **2019,** *141*, 9764-9768.
51. Jun, T.; Sim, K.; Iimura, S.; Sasase, M.; Kamioka, H.; Kim, J.; Hosono, H., Lead-Free Highly Efficient Blue-Emitting Cs3Cu2I5 with 0D Electronic Structure, *Adv. Mater.* **2018,** *30*, 1804547.
52. Spanopoulos, I.; Ke, W.; Stoumpos, C. C.; Schueller, E. C.; Kontsevoi, O. Y.; Seshadri, R.; Kanatzidis, M. G., Unraveling the Chemical Nature of the 3D "Hollow" Hybrid Halide Perovskites, *J. Am. Chem. Soc.* **2018,** *140*, 5728-5742.
53. Spanopoulos, I.; Hadar, I.; Ke, W.; Tu, Q.; Chen, M.; Tsai, H.; He, Y.; Shekhawat, G.; Dravid, V. P.; Wasielewski, M. R.; Mohite, A. D.; Stoumpos, C. C.; Kanatzidis, M. G., Uniaxial Expansion of the 2D Ruddlesden–Popper Perovskite Family for Improved Environmental Stability, *J. Am. Chem. Soc.* **2019,** *141*, 5518-5534.
54. Saidaminov, M. I.; Abdelhady, A. L.; Maculan, G.; Bakr, O. M., Retrograde solubility of formamidinium and methylammonium lead halide perovskites enabling rapid single crystal growth, *Chem. Commun.* **2015,** *51*, 17658-17661.
55. Li, X.; Hoffman, J.; Ke, W.; Chen, M.; Tsai, H.; Nie, W.; Mohite, A. D.; Kepenekian, M.; Katan, C.; Even, J.; Wasielewski, M. R.; Stoumpos, C. C.; Kanatzidis, M. G., Two-Dimensional Halide Perovskites Incorporating Straight Chain Symmetric Diammonium Ions, (NH3CmH2mNH3)(CH3NH3)n−1PbnI3n+1 (m = 4–9; n = 1–4), *J. Am. Chem. Soc.* **2018,** *140*, 12226-12238.
56. Mascal, M., A statistical analysis of halide · · · H–A (A = OR, NR2, N+R3) hydrogen bonding interactions in the solid state, *Journal of the Chemical Society, Perkin Transactions 2* **1997**, 1999-2001.
57. Giorgi, G.; Fujisawa, J.-I.; Segawa, H.; Yamashita, K., Small Photocarrier Effective Masses Featuring Ambipolar Transport in Methylammonium Lead Iodide Perovskite: A Density Functional Analysis, *J. Phys. Chem. Lett.* **2013,** *4*, 4213-4216.
58. Umari, P.; Mosconi, E.; De Angelis, F., Relativistic GW calculations on CH3NH3PbI3 and CH3NH3SnI3 Perovskites for Solar Cell Applications, *Sci. Rep.* **2014,** *4*, 4467.
59. Wang, Z.; Ganose, Alex M.; Niu, C.; Scanlon, D. O., First-principles insights into tin-based two-dimensional hybrid halide perovskites for photovoltaics, *J. Mater. Chem. A* **2018,** *6*, 5652-5660.
60. Yin, W.-J.; Shi, T.; Yan, Y., Unique Properties of Halide Perovskites as Possible Origins of the Superior Solar Cell Performance, *Adv. Mater.* **2014,** *26*, 4653-4658.
61. Yaffe, O.; Guo, Y.; Tan, L. Z.; Egger, D. A.; Hull, T.; Stoumpos, C. C.; Zheng, F.; Heinz, T. F.; Kronik, L.; Kanatzidis, M. G.; Owen, J. S.; Rappe, A. M.; Pimenta, M. A.; Brus, L. E., Local Polar Fluctuations in Lead Halide Perovskite Crystals, *Phys. Rev. Lett.* **2017,** *118*, 136001.
62. Kaltzoglou, A.; Manolis, G. K.; Elsenety, M. M.; Koutselas, I.; Psycharis, V.; Kontos, A. G.; Falaras, P., Synthesis and Characterization of Lead-Free (CH3)3SSnI3 1-D Perovskite, *J. Electron. Mater.* **2019,** *48*, 7533-7538.
63. Taylor, M. J., Raman spectrum of the [SnI3]− ion and other halogenostannate(II) complexes including mixed halides, *Journal of Raman Spectroscopy* **1989,** *20*, 663-666.
64. Smith, M. D.; Watson, B. L.; Dauskardt, R. H.; Karunadasa, H. I., Broadband Emission with a Massive Stokes Shift from Sulfonium Pb–Br Hybrids, *Chem. Mater.* **2017,** *29*, 7083-7087.
65. Seth, S.; Samanta, A., Photoluminescence of Zero-Dimensional Perovskites and Perovskite-Related Materials, *J. Phys. Chem. Lett.* **2018,** *9*, 176-183.
66. Zhou, L.; Liao, J. F.; Huang, Z. G.; Wei, J. H.; Wang, X. D.; Li, W. G.; Chen, H. Y.; Kuang, D. B.; Su, C. Y., A Highly Red-Emissive Lead-Free Indium-Based Perovskite Single Crystal for Sensitive Water Detection, *Angew. Chem. Int. Ed.* **2019,** *58*, 5277-5281.
67. Booker, E. P.; Thomas, T. H.; Quarti, C.; Stanton, M. R.; Dashwood, C. D.; Gillett, A. J.; Richter, J. M.; Pearson, A. J.; Davis, N. J. L. K.; Sirringhaus, H.; Price, M. B.; Greenham, N. C.; Beljonne, D.; Dutton, S. E.; Deschler, F., Formation of Long-Lived Color Centers for Broadband Visible Light Emission in Low-Dimensional Layered Perovskites, *J. Am. Chem. Soc.* **2017,** *139*, 18632-18639.
68. Smith, M. D.; Jaffe, A.; Dohner, E. R.; Lindenberg, A. M.; Karunadasa, H. I., Structural origins of broadband emission from layered Pb–Br hybrid perovskites, *Chemical Science* **2017,** *8*, 4497-4504.

69. Bowers, M. J.; McBride, J. R.; Rosenthal, S. J., White-Light Emission from Magic-Sized Cadmium Selenide Nanocrystals, *J. Am. Chem. Soc.* **2005,** *127*, 15378-15379.
70. Cortecchia, D.; Yin, J.; Petrozza, A.; Soci, C., White light emission in low-dimensional perovskites, *J. Mater. Chem. C* **2019,** *7*, 4956-4969.
71. Pimputkar, S.; Speck, J. S.; DenBaars, S. P.; Nakamura, S., Prospects for LED lighting, *Nature Photonics* **2009,** *3*, 180.
72. Harwell, J. R.; Baikie, T. K.; Baikie, I. D.; Payne, J. L.; Ni, C.; Irvine, J. T. S.; Turnbull, G. A.; Samuel, I. D. W., Probing the energy levels of perovskite solar cells via Kelvin probe and UV ambient pressure photoemission spectroscopy, *Phys. Chem. Chem. Phys.* **2016,** *18*, 19738-19745.
73. Spanopoulos, I.; Ke, W.; Stoumpos, C. C.; Schueller, E. C.; Kontsevoi, O. Y.; Seshadri, R.; Kanatzidis, M. G., Unraveling the Chemical Nature of the 3D "Hollow" Hybrid Halide Perovskites, *J. Am. Chem. Soc.* **2018,** *140*, 5728-5742.
74. Chen, T.; Chen, W.-L.; Foley, B. J.; Lee, J.; Ruff, J. P. C.; Ko, J. Y. P.; Brown, C. M.; Harriger, L. W.; Zhang, D.; Park, C.; Yoon, M.; Chang, Y.-M.; Choi, J. J.; Lee, S.-H., Origin of long lifetime of band-edge charge carriers in organic–inorganic lead iodide perovskites, *Proc. Natl. Acad. Sci.* **2017,** *114*, 7519-7524.
75. Lin, R.; Guo, Q.; Zhu, Q.; Zhu, Y.; Zheng, W.; Huang, F., All-Inorganic CsCu2I3 Single Crystal with High-PLQY (≈15.7%) Intrinsic White-Light Emission via Strongly Localized 1D Excitonic Recombination, *Adv. Mater.* **2019**, 1905079.
76. Tongay, S.; Suh, J.; Ataca, C.; Fan, W.; Luce, A.; Kang, J. S.; Liu, J.; Ko, C.; Raghunathanan, R.; Zhou, J.; Ogletree, F.; Li, J.; Grossman, J. C.; Wu, J., Defects activated photoluminescence in two-dimensional semiconductors: interplay between bound, charged, and free excitons, *Sci. Rep.* **2013,** *3*, 2657.
77. Reshchikov, M. A.; Morkoç, H., Luminescence properties of defects in GaN, *J. Appl. Phys.* **2005,** *97*, 061301.
78. Meggiolaro, D.; Motti, S. G.; Mosconi, E.; Barker, A. J.; Ball, J.; Andrea Riccardo Perini, C.; Deschler, F.; Petrozza, A.; De Angelis, F., Iodine chemistry determines the defect tolerance of lead-halide perovskites, *Energ Environ Sci* **2018,** *11*, 702-713.
79. Paternò, G. M.; Mishra, N.; Barker, A. J.; Dang, Z.; Lanzani, G.; Manna, L.; Petrozza, A., Broadband Defects Emission and Enhanced Ligand Raman Scattering in 0D Cs3Bi2I9 Colloidal Nanocrystals, *Adv. Funct. Mater.* **2019,** *29*, 1805299.
80. Underwood, D. F.; Kippeny, T.; Rosenthal, S. J., Ultrafast Carrier Dynamics in CdSe Nanocrystals Determined by Femtosecond Fluorescence Upconversion Spectroscopy, *The Journal of Physical Chemistry B* **2001,** *105*, 436-443.
81. De Santi, C.; Dal Lago, M.; Buffolo, M.; Monti, D.; Meneghini, M.; Meneghesso, G.; Zanoni, E., Failure causes and mechanisms of retrofit LED lamps, *Microelectronics Reliability* **2015,** *55*, 1765-1769.
82. Zhang, H. In *Developing highly reliable LED luminaires for high temperature applications using AC-direct driving LED technology*, 2018 IEEE Applied Power Electronics Conference and Exposition (APEC), 4-8 March 2018; 2018; pp 3466-3470.

Figures

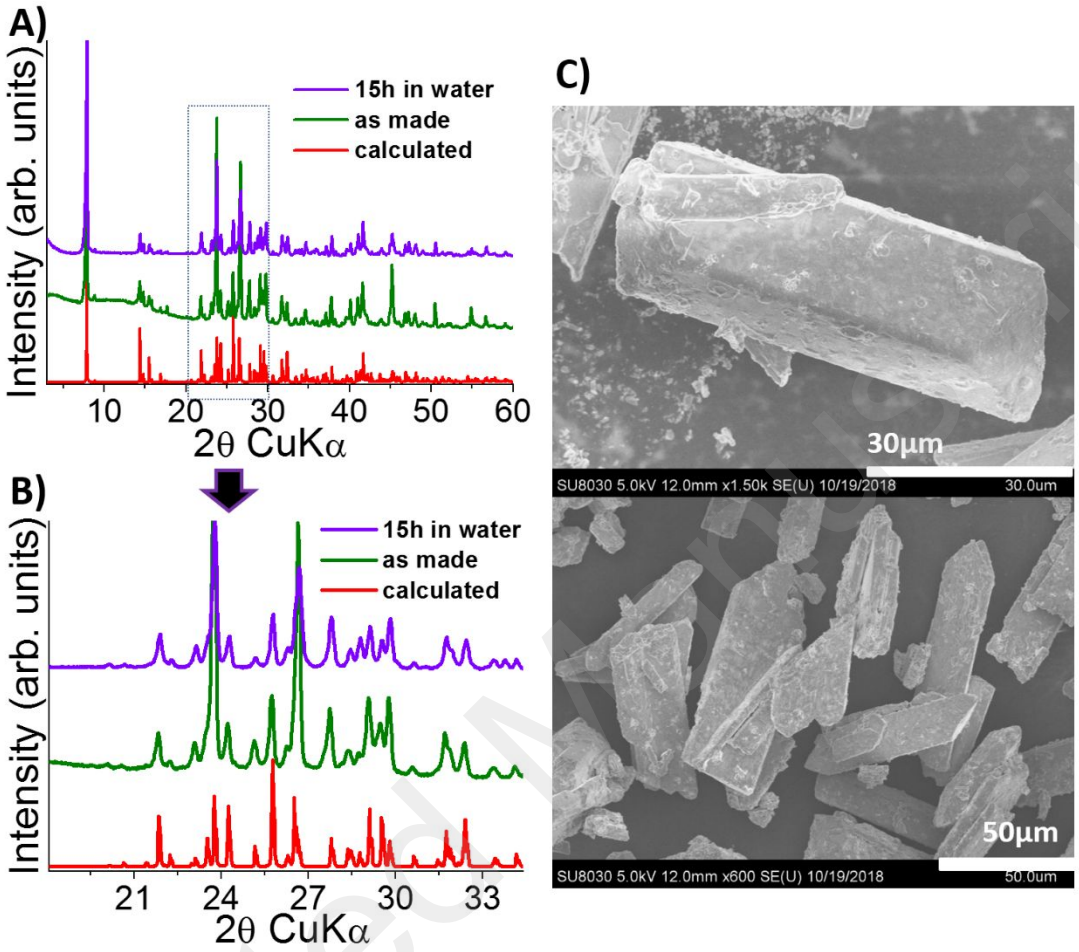

Figure 1. A) Comparison of the PXRD patterns for the as made $(DAO)Sn_2I_6$ crystals and the water treated ones, to the calculated pattern based from the solved single crystal structure and B) zoom into the highlighted area of the PXRD patterns from 20° to 34° 2θ verifying the high crystallinity and phase purity of the water treated sample. C) Representative SEM images of the as made $(DAO)Sn_2I_6$ single crystals.

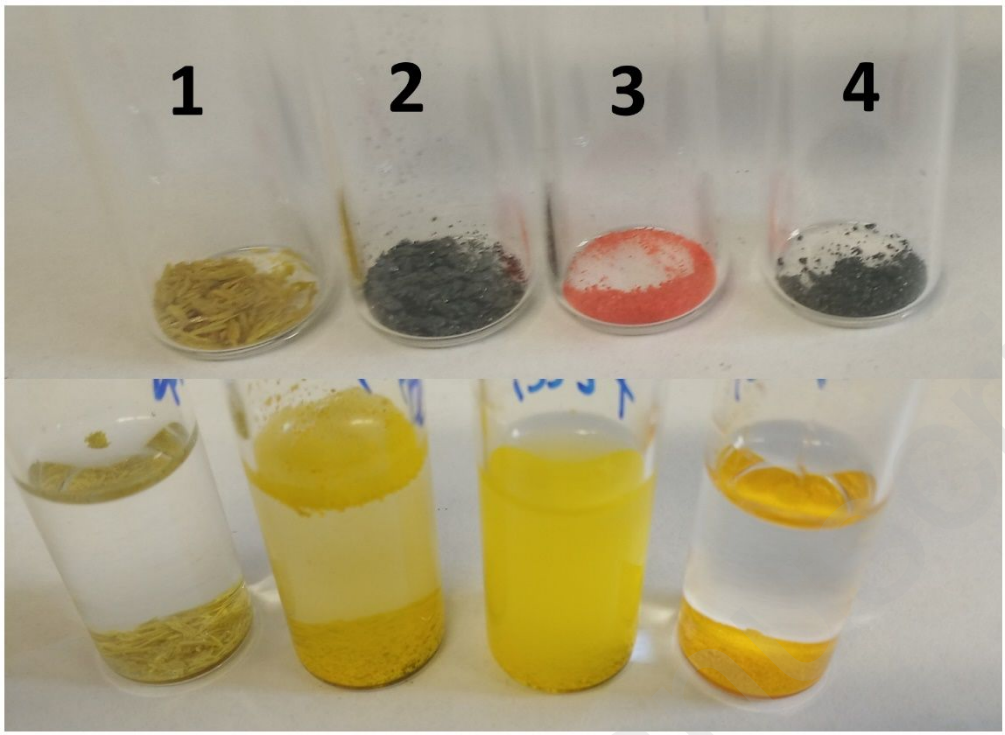

Figure 2. Water stability test. Top: Single crystals of (DAO)Sn_2I_6 (1) along with some of the most stable in air Pb based perovskites, such as the 2D $(HA)_2(MA)_3Pb_4I_{13}$ (2) the highly "hollow" 3D $(MA)_{0.56}(en)_{0.44}(Pb)_{0.692}(I)_{2.824}$ (3), and the pristine 3D $MAPbI_3$ (4) for comparison. Bottom: The corresponding crystals immersed in water. Compounds (2), (3) and (4) decomposed immediately, while (1) is structurally intact even after 15 hours.

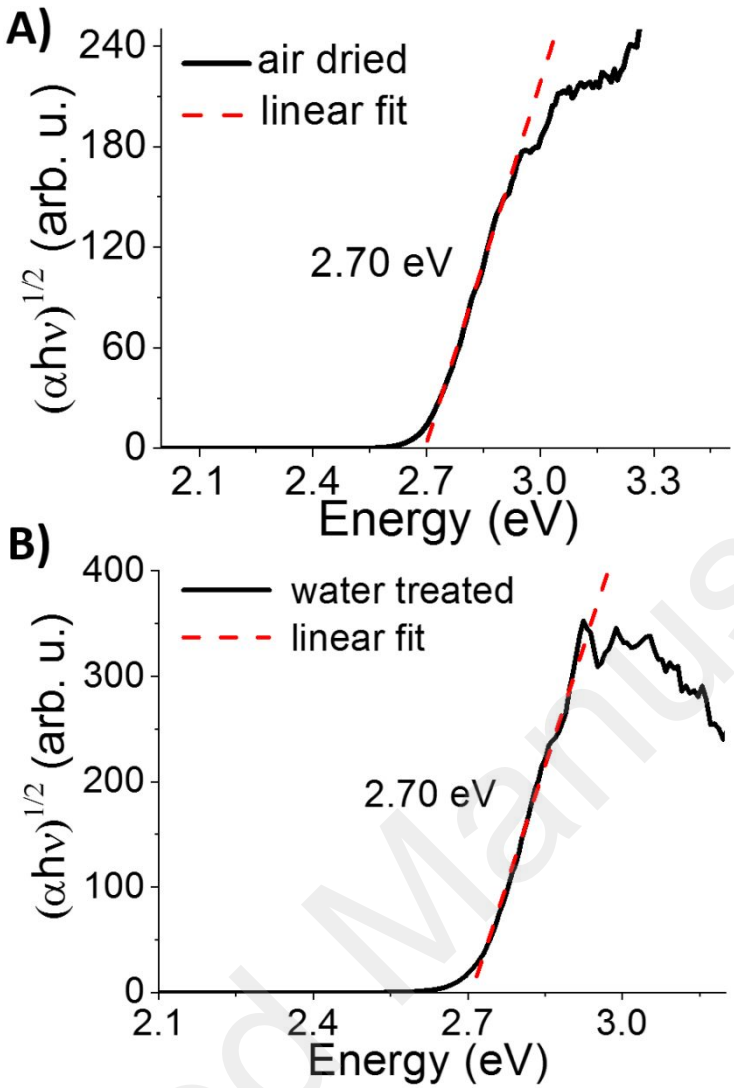

Figure 3. Tauc plot and determined band gap for (A) the fresh crystals and (B) the water treated ones.

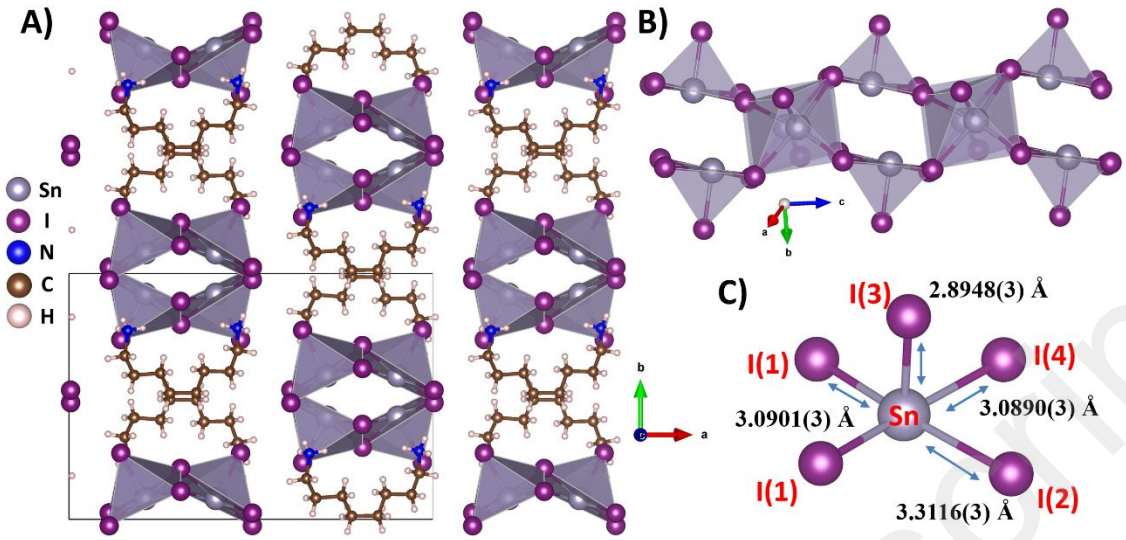

Figure 4. A) Part of the 1D structure of (DAO)Sn_2I_6 at RT, looking down the *c*-axis. B) Representation of the 1D double inorganic chain based on $[SnI_5]^{3-}$ moieties. C) The distorted square pyramidal geometry of the Sn^{2+} cations of the inorganic chain, along with the corresponding Sn-I bond lengths and atom numbers.

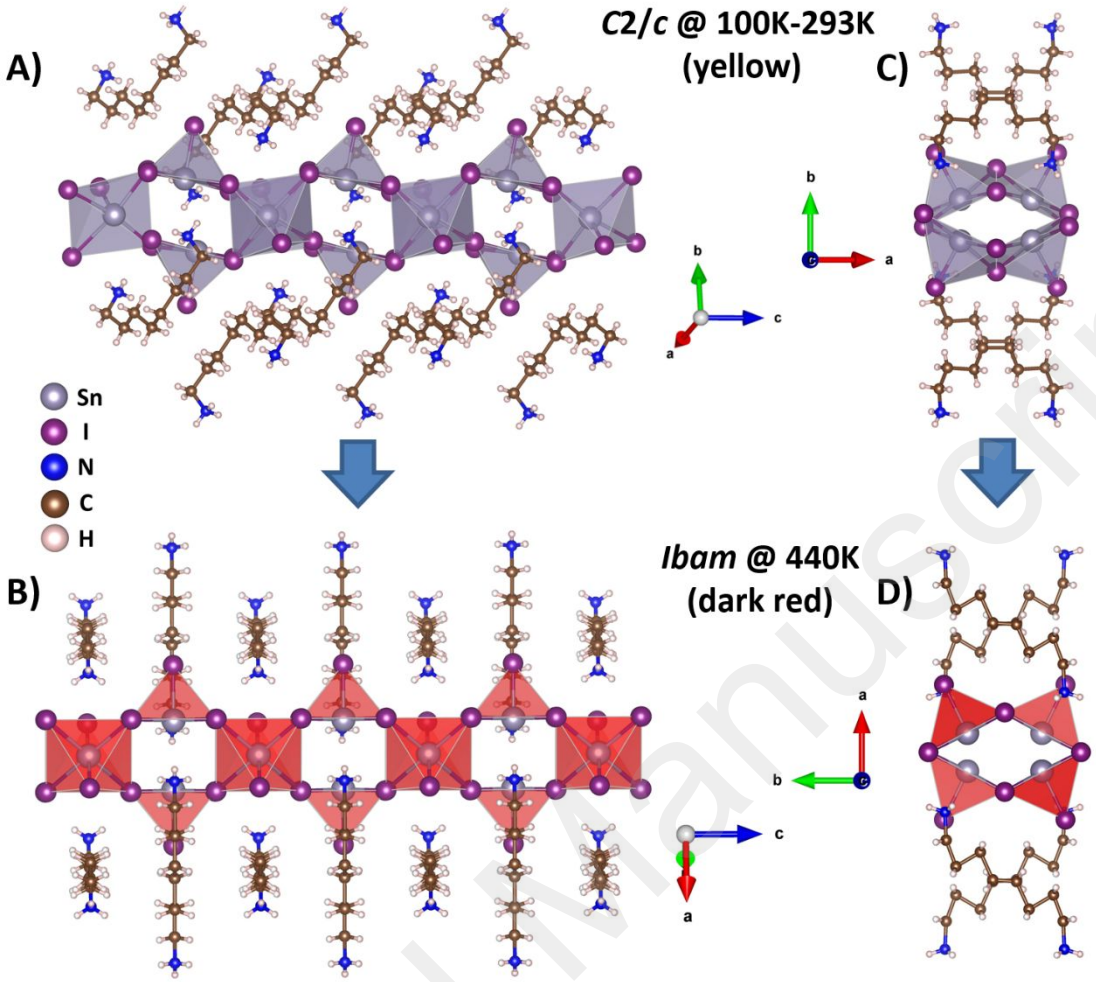

Figure 5. The recorded temperature dependent phase transition of (DAO)Sn_2I_6. A) The yellow crystals crystallize at the monoclinic *C*2/*c* space group at 293K, B) while at 440K the structure exhibits a profound phase transition to the orthorhombic phase (*Ibam* space group) accompanied by less distorted, highly oriented organic and inorganic parts and a crystal color change from yellow to dark red. C) Part of the RT and D) HT structures viewing along *c*-axis.

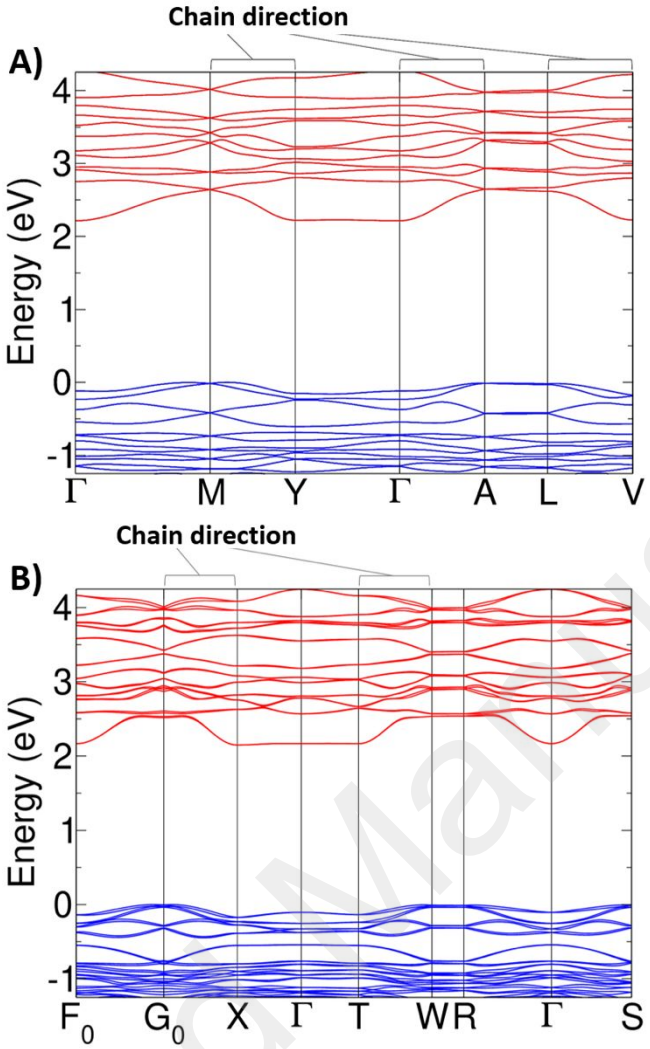

Figure 6. Electronic band structures for A) RT yellow crystals of $(DAO)Sn_2I_6$ and as well as for B) the high temperature red crystals.

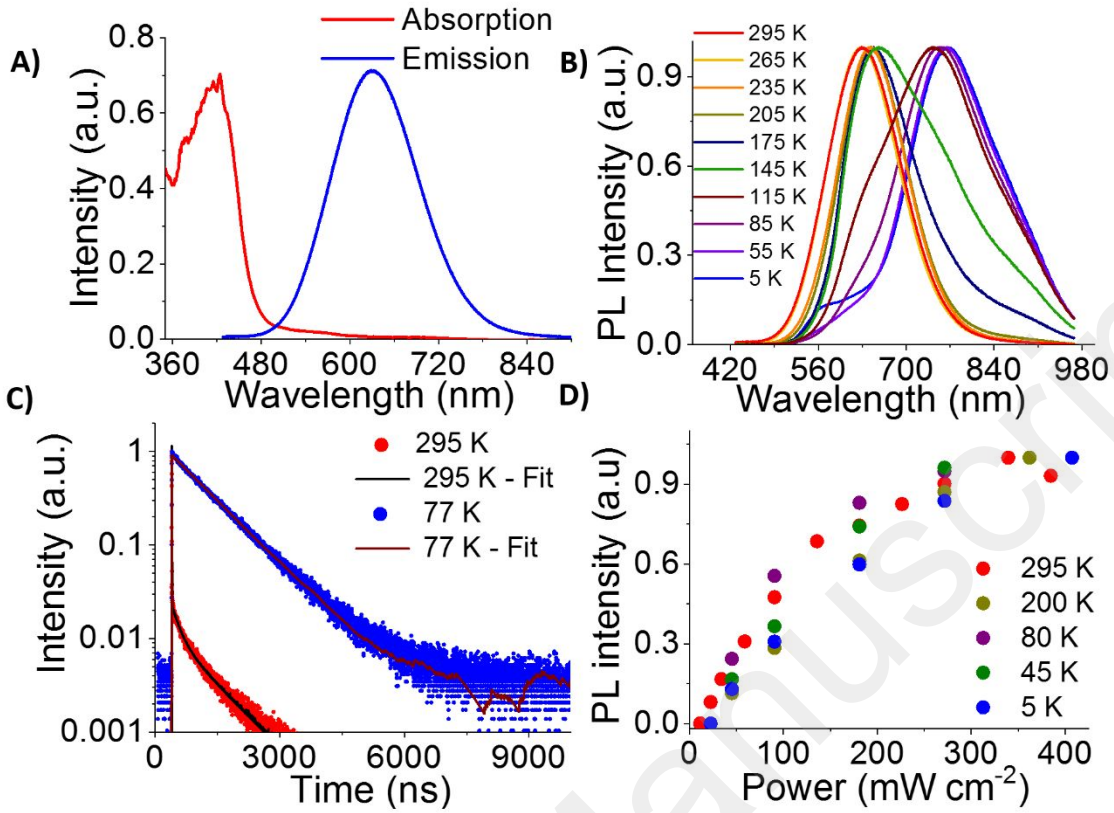

Figure 7. A) The recorded absorption and emission spectra of compound $(DAO)Sn_2I_6$, B) temperature dependent PL measurements from 295K to 5K, C) Time-resolved photoluminescence decay at 77K and 295K, D) Emission intensity versus excitation power at various temperatures, revealing the saturation of PL intensity with increasing power.

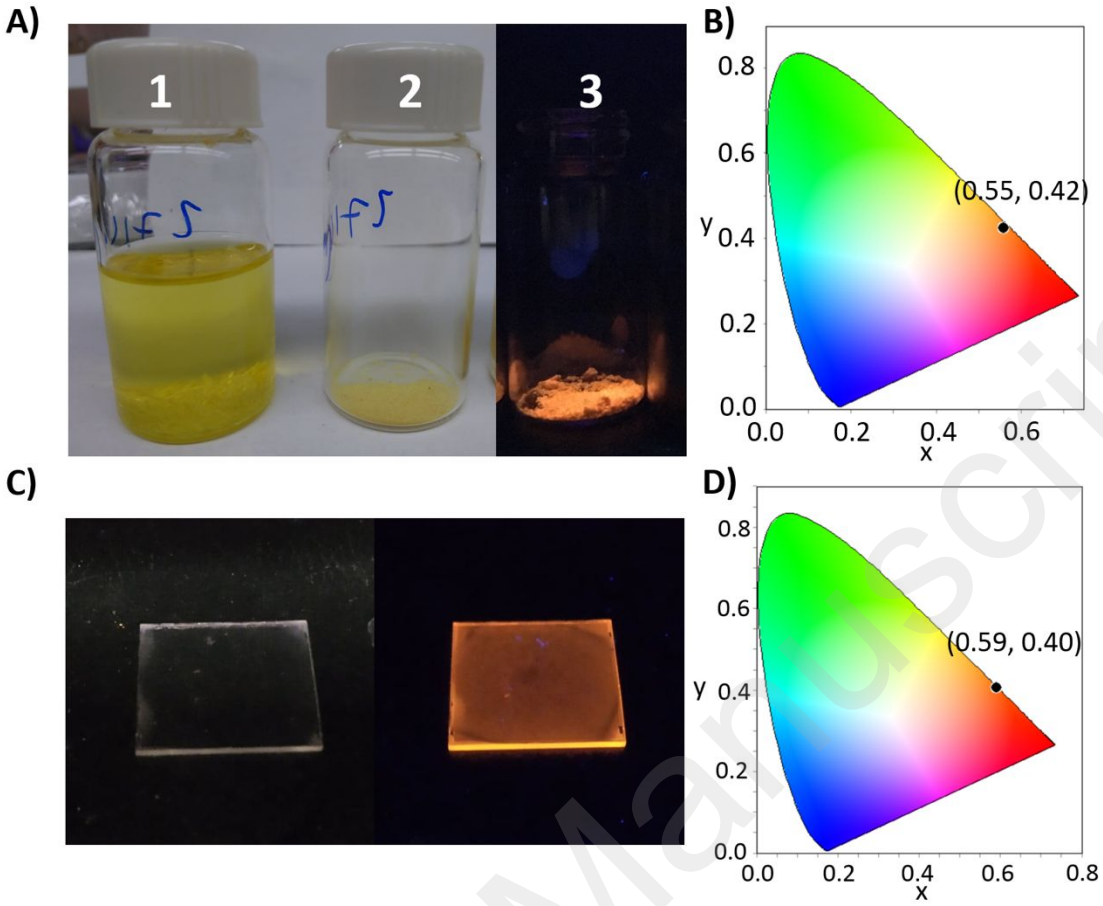

Figure 8. A) Photographs of (1) as made single crystals in the mother liquor of hydrogen iodide and hypophosphorous acid, (2) dried crystals under ambient light, and (3) and under UV light. B) CIE chromaticity coordinates for $(DAO)Sn_2I_6$. C) Photographs of fabricated thin film under ambient light and under UV light. D) CIE chromaticity coordinates for the thin film emission.

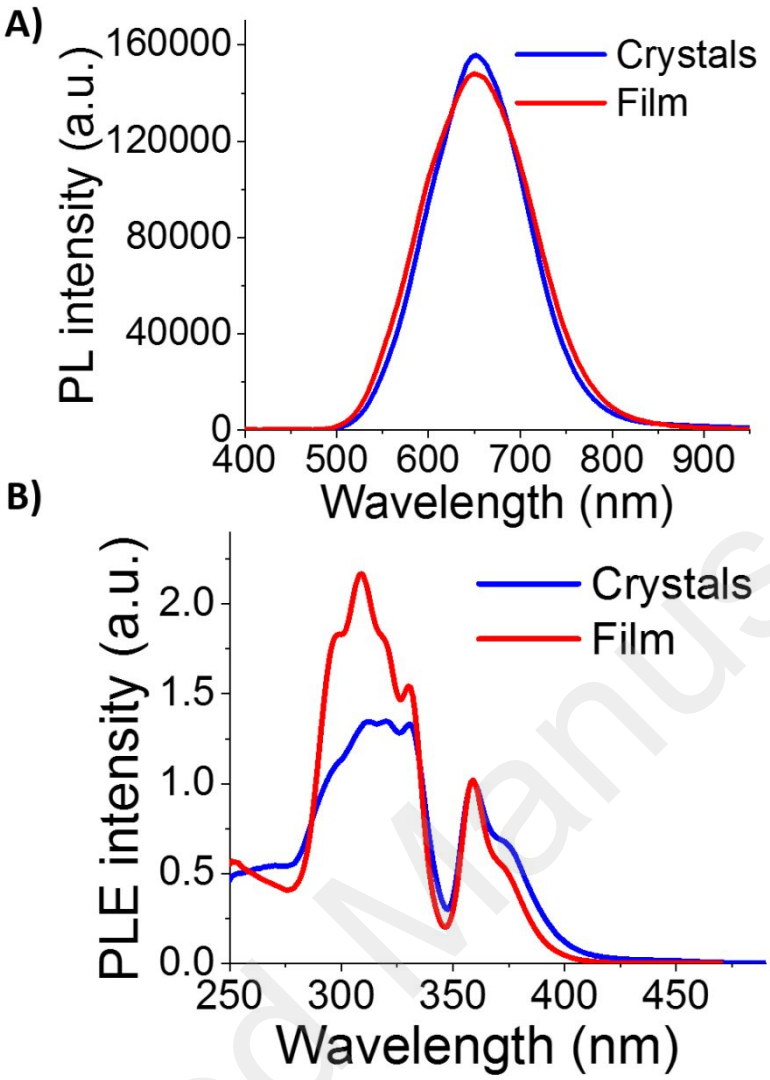

Figure 9. Comparison of (A) PL emission spectra and (B) PLE spectra for (DAO)Sn_2I_6 single crystals and thin film.

Table 1. Crystal and Structure Refinement Data for $(DAO)Sn_2I_6$ at 100K, 293K and 440K.

Temperature	**100K**	**293K**	**440K**
Crystal system	monoclinic	monoclinic	orthorhombic
Space group	*C*2/*c*	*C*2/*c*	*Ibam*
Unit cell dimensions	a = 21.0227(12) Å, α = 90° b = 13.4267(8) Å, β = 108.8167(19)° c = 8.6803(5) Å, γ = 90°	a = 21.1574(8) Å, α = 90° b = 13.5267(5) Å, β = 108.8895(17)° c = 8.7500(3) Å, γ = 90°	a = 13.7210(3) Å, α = 90° b = 20.3857(6) Å, β = 90° c = 8.8553(8) Å, γ = 90°
Volume	2319.2(2) $Å^3$	2369.30(15) $Å^3$	2476.9(2) $Å^3$
Z	4	4	4
Density (calculated)	3.2796 g/cm^3	3.2103 g/cm^3	3.0708 g/cm^3
Independent reflections	4230 [R_{int} = 0.0395]	5392 [R_{int} = 0.0378]	1304 [R_{int} = 0.0294]
Completeness to θ = 29.33°	98%	98%	99%
Data / restraints / parameters	4230 / 0 / 58	5392 / 0 / 58	1304 / 3 / 38
Goodness-of-fit	1.42	1.35	2.82
Final R indices [I>2σ(I)]	R_{obs} = 0.0171, wR_{obs} = 0.0516	R_{obs} = 0.0287, wR_{obs} = 0.0718	R_{obs} = 0.0472, wR_{obs} = 0.1194
R indices [all data]	R_{all} = 0.0177, wR_{all} = 0.0519	R_{all} = 0.0380, wR_{all} = 0.0764	R_{all} = 0.0662, wR_{all} = 0.1249
Largest diff. peak and hole	0.61 and -0.61 $e \cdot Å^{-3}$	0.99 and -0.64 $e \cdot Å^{-3}$	0.86 and -0.48 $e \cdot Å^{-3}$

$R = \Sigma||F_o|-|F_c|| / \Sigma|F_o|$, $wR = (\Sigma[w(|F_o|^2 - |F_c|^2)^2] / \Sigma[w(|F_o|^4)])^{1/2}$ and $w=1/(\sigma^2(I)+0.0004I^2)$

Table 2. Photophysical properties of the bulk crystals and the assembled thin film of the $(DAO)Sn_2I_6$ compound. (τ_{av} is the average PL lifetime).

$(DAO)Sn_2I_6$	**T(K)**	**PLQY (%)**	**τ_{av} (ns)**	**FWHM (nm)**	**CRI**	**CCT (K)**	**CIE**
Crystals	298K	20.3	582	142	75	1822	(0.55,0.42)
Film	298K	36	1114	145	74	1529	(0.59,0.40)

Table of Contents Graphic